

# Evolution from quantum anomalous Hall insulator to heavy-fermion semimetal in magic-angle twisted bilayer graphene

Cheng Huang,<sup>1</sup> Xu Zhang,<sup>1</sup> Gaopei Pan,<sup>2,3</sup> Heqiu Li,<sup>4</sup> Kai Sun,<sup>5,\*</sup> Xi Dai,<sup>6,†</sup> and Ziyang Meng<sup>1,‡</sup>

<sup>1</sup>*Department of Physics and HKU-UCAS Joint Institute of Theoretical and Computational Physics, The University of Hong Kong, Pokfulam Road, Hong Kong SAR, China*

<sup>2</sup>*Beijing National Laboratory for Condensed Matter Physics and Institute of Physics, Chinese Academy of Sciences, Beijing 100190, China*

<sup>3</sup>*School of Physical Sciences, University of Chinese Academy of Sciences, Beijing 100049, China*

<sup>4</sup>*Department of Physics, University of Toronto, Toronto, Ontario M5S 1A7, Canada*

<sup>5</sup>*Department of Physics, University of Michigan, Ann Arbor, Michigan 48109, USA*

<sup>6</sup>*Department of Physics, Hong Kong University of Science and Technology, Kowloon, Hong Kong SAR, China*

(Dated: May 30, 2023)

The ground states of twisted bilayer graphene (TBG) at chiral and flat-band limit with integer fillings are known from exact solutions, while their dynamical and thermodynamical properties are revealed by unbiased quantum Monte Carlo (QMC) simulations. However, to elucidate experimental observations of correlated metallic, insulating and superconducting states and their transitions, investigations on realistic, or non-chiral cases are vital. Here we employ momentum-space QMC method to investigate the evolution of correlated states in magic-angle TBG away from chiral limit at charge neutrality with polarized spin/valley, which approximates to an experimental case with filling factor  $\nu = -3$ . We find that the ground state evolves from quantum anomalous Hall insulator into an intriguing correlated semi-metallic state as AA hopping strength reaches experimental values. Such a state resembles the recently proposed heavy-fermion representations with localized electrons residing at AA stacking regions and delocalized electrons itinerating via AB/BA stacking regions. The spectral signatures of the localized and itinerant electrons in the heavy-fermion semimetal phase are revealed, with the connection to experimental results being discussed.

**Introduction.**— Flat bands of non-interacting magic-angle twisted bilayer graphene (TBG) can be readily characterized by tight-binding [1, 2] or continuous (BM) [3] models. Yet, in such deceptively simple systems, it is the interplay of long-range Coulomb interaction, quantum metric of flat-band wavefunction and the extremely high tunability, by twisting angles, gating and dielectric environment, that gives rise to a plethora of novel quantum states including correlated insulator [4–14], unconventional metal with linear- $T$  resistivity, superconductor and beyond [15–20], the underlying principles and mechanisms of which, are still under intensive investigations.

Among these efforts, exact solutions [14, 21–24], mean-field analyses [23, 25–31], density matrix renormalization group (DMRG) investigations [32, 33], and momentum-space quantum Monte Carlo (QMC) simulations [34–38] reveal that the TBG model of the first magic angle ( $1.08^\circ$ ) with Coulomb interaction projected into the flat bands possesses a quantum anomalous Hall (QAH) ground state with Chern number  $C = 1$ , at chiral (AA stacking hopping  $u_0 = 0$ ) and flat-band limit (ignoring kinetic energy) with filling factor  $\nu = \pm 3$  (we denote the band filling factor  $\nu = 4n/n_s$ , where  $n$  is the carrier density normalized to  $n_s$ , the density of the fully filled fourfold spin/valley degenerate bands). For the same system away from chiral limit, which means  $u_0 > 0$  (can be varied experimentally by twisting angle, temperature, strain, magnetic field, or pressure, etc [16, 18]), a DMRG investigation suggests its ground state remains Chern polarized until  $u_0/u_1 \approx 0.8$  (AB/BA stacking hopping  $u_1 \approx 110$  meV), beyond which competing states such as  $C_2\mathcal{T}$  nematic and  $C_2\mathcal{T}$  stripe phases emerge [32]. However, another DMRG work indicates the ground state is a nematic  $C_2\mathcal{T}$  semimetal state when  $u_0/u_1 > 0.8$  [33], while a

recent Hartree-Fock mean-field study suggests the then state to be monolayer-CDW insulating [28].

Experimentally, magic-angle (from now on magic-angle refers to the first magic angle) TBG at  $\nu = -3$  is found to be metallic (or semi-metallic considering carrier concentration) with electron localization, neighboring to a superconducting phase, while that of  $\nu = 3$  is semiconducting or insulating [6, 8, 9, 11, 39–41], when  $u_1$  is around 110 meV [42–44] and  $u_0$  is realistically around 0.8 of  $u_1$  [45–47] due to lattice relaxation. The difference between the experimentally observed phases (especially for  $\nu = -3$ ) and the above theoretical proposals arises probably from the limitations of theoretical methods used in the TBG model investigations.

To understand and clarify the discrepancies between theories and experiments, in this work, we apply the unbiased momentum-space QMC simulation [34–38, 48], supplemented with exact diagonalization [49], to systematically investigate the evolution of the correlated state as a function of  $u_0$  of magic-angle TBG at  $\nu = -3$  with the Coulomb interaction projected into flat bands. Our results show both the single-particle gap and Chern number polarization decrease with increasing  $u_0$ , and eventually vanish when  $u_0 \approx 0.7u_1$ , where a semimetallic state emerges. This semimetallic state is gapless in the vicinity of  $\Gamma$  point of the moiré Brillouin zone. In real space it has localized states at the AA stacking region and itinerant states at the AB/BA stacking regions of the moiré unit cell – a solid analog to the experiments [8, 9] and recently found heavy-fermion representations of the TBG system, with AA stacking regions proposed to hold states of localized flat bands ( $f$  electrons) and AB/BA stacking regions bridging itinerant states ( $c$  electrons) [31, 50–55].

Since our model has no prior heavy-fermion representation in the first place but only the approximation of projecting the Coulomb interaction into the flat bands, our observation, the evolution from QAH insulator to heavy-fermion semimetal at  $\nu = -3$ , provides the first unbiased and unifying interpretation of the ground state of magic-angle TBG from topological Mott insulator (at chiral limit) emerging from the correlated flat bands to the semi-metallic state (non-chiral, actual) with topological heavy-fermion characters.

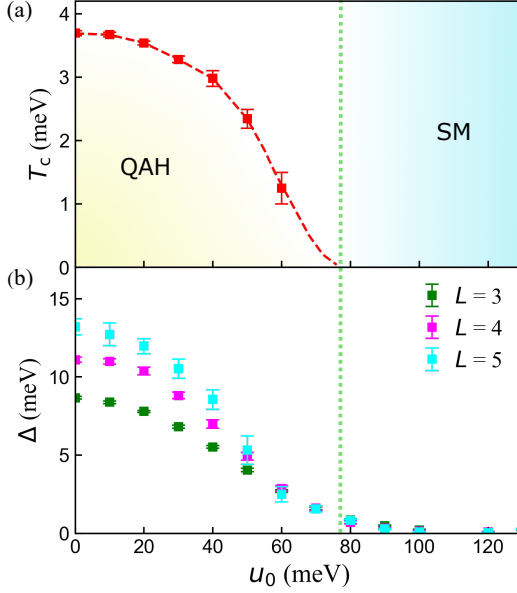


FIG. 1. **QAH insulator to heavy-fermion semimetal transition away from chiral limit in  $\nu = -3$  magic-angle TBG.** (a) QAH transition temperature ( $T_c$ ) and (b) single-particle gap ( $\Delta$ ) vary with increasing  $u_0$ . The  $T_c$ -s are determined from the time-reversal symmetry breaking with 2D Ising exponents, as shown in Fig. S7 in the Supplementary Materials (SM) [56]. The single-particle gaps are obtained by fitting the exponential decay of imaginary time Green's functions of  $\Gamma$  point with finite sizes ( $L = 3, 4, 5$ ) and finite temperature ( $T = 3$  meV) simulations. The imaginary time data with the fitting curves are shown in Fig. S4 in SM [56].

**Model and Method.**— As shown in Fig. S1, the twisted bilayer graphene generates a morié pattern, with a periodic area consisting of one AA, one AB, and one BA stacking regions. Here the periodic area is dubbed morié unit cell (mUC), and its Brillouin zone is dubbed morié Brillouin zone (mBZ). The nearest distance between carbon atoms in each graphene layer is  $a = 1.42 \text{ \AA}$ , and the lattice vectors of mUC are  $\mathbf{a}_{M1}, \mathbf{a}_{M2}$ , with  $|\mathbf{a}_{M1/M2}| = \sqrt{3}a/[2\sin(\theta/2)]$ , while the lattice vectors of mBZ are  $\mathbf{G}_1$  and  $\mathbf{G}_2$ , with  $|\mathbf{G}_{1/2}| = 8\pi\sin(\theta/2)/(3a)$ .  $\mathbf{K}_1^\eta$  and  $\mathbf{K}_2^\eta$  are Dirac points from the top (1) and bottom (2) layers, respectively, and  $\eta = \pm$  labels the two valleys. Schematics of hopping patterns are also shown in the right panel of Fig. S1. In this work, we consider the system with the first magic angle ( $\theta = 1.08^\circ$ ).

In principle, the Hamiltonian of TBG contains kinetic and

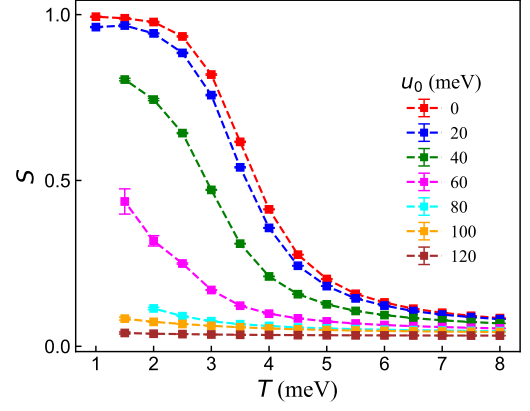


FIG. 2. **Chern number polarization  $S$  as functions of  $u_0$  and  $T$ .** The results are obtained from  $L = 4$  system, and the  $T$  for each  $u_0$  reaches the temperature as low as possible, with  $\langle \text{sign} \rangle$  lowering than 0.05. It is clear that as  $u_0$  increases, the value of  $S$  at low temperature drops quickly and a transition between QAH and SM happens at  $u_0 \approx 80$  meV.

interaction parts,  $H = H_0 + H_I$ . The kinetic part is

$$H_0 = \sum_{\mathbf{k}, \mathbf{G}, \mathbf{G}', \eta, s} \mathbf{c}_{\mathbf{k}, \mathbf{G}, \eta, s}^\dagger H^{\eta, s}(\mathbf{k}, \mathbf{G}, \mathbf{G}') \mathbf{c}_{\mathbf{k}, \mathbf{G}', \eta, s}, \quad (1)$$

where

$$H^{\eta, s}(\mathbf{k}, \mathbf{G}, \mathbf{G}') = \delta_{\mathbf{k}_1, \mathbf{k}_2} \hbar v_F \begin{pmatrix} -(\mathbf{k}_1 - \mathbf{K}_1^\eta) \cdot \boldsymbol{\sigma}^\eta & 0 \\ 0 & -(\mathbf{k}_1 - \mathbf{K}_2^\eta) \cdot \boldsymbol{\sigma}^\eta \end{pmatrix} + \begin{pmatrix} 0 & T_1^\eta \\ T_2^{\eta\dagger} & 0 \end{pmatrix} \quad (2)$$

is the BM model [3] with

$$T_l^\eta = \begin{pmatrix} u_0 & u_1 \\ u_1 & u_0 \end{pmatrix} \delta_{\mathbf{k}_1, \mathbf{k}_2} + \begin{pmatrix} u_0 & u_1 e^{-i\frac{2\pi}{3}\eta} \\ u_1 e^{i\frac{2\pi}{3}\eta} & u_0 \end{pmatrix} \delta_{\mathbf{k}_1, \mathbf{k}_2 + (-1)^l \eta \mathbf{G}_1} + \begin{pmatrix} u_0 & u_1 e^{i\frac{2\pi}{3}\eta} \\ u_1 e^{-i\frac{2\pi}{3}\eta} & u_0 \end{pmatrix} \delta_{\mathbf{k}_1, \mathbf{k}_2 + (-1)^l \eta (\mathbf{G}_1 + \mathbf{G}_2)}. \quad (3)$$

Here  $\mathbf{k}$  is a momentum in mBZ,  $\mathbf{G}$  is a momentum cutoff for  $\mathbf{k}$ , as  $\mathbf{k}_1 = \mathbf{k} + \mathbf{G}$  and  $\mathbf{k}_2 = \mathbf{k} + \mathbf{G}'$ , and  $\mathbf{G}, \mathbf{G}' \in \{N_1 \mathbf{G}_1 + N_2 \mathbf{G}_2\}$ , with  $N_1$  and  $N_2$  being integers and a constraint  $|\mathbf{G}|, |\mathbf{G}'| \leq 4|\mathbf{G}_1|$  being applied.  $\mathbf{c}_{\mathbf{k}, \mathbf{G}, \eta, s}^\dagger$  is a  $1 \times 4$  vector of creation operators for layers (1, 2) and sublattices (A, B), with  $s$  specifying spins ( $\uparrow, \downarrow$ ) and  $v_F$  being the Fermi velocity (here we choose  $\hbar v_F / (\sqrt{3}a) = 2.37745$  eV), and  $\boldsymbol{\sigma}^\eta = (\eta \sigma_x, \sigma_y)$ , where  $\sigma_x$  and  $\sigma_y$  are Pauli matrices corresponding to different sublattices. The first part of  $H^{\eta, s}(\mathbf{k}, \mathbf{G}, \mathbf{G}')$  stands for intra-layer hopping of top (1) layer and bottom (2) layer, respectively, and the second part stands for inter-layer hopping, which is actually the morié potential.

The interaction part is

$$H_I = \frac{1}{2\Omega} \sum_{|\mathbf{q} + \mathbf{G}| \neq 0} V(\mathbf{q} + \mathbf{G}) \delta \rho_{\mathbf{q} + \mathbf{G}} \delta \rho_{-\mathbf{q} - \mathbf{G}}, \quad (4)$$

where

$$\delta\rho_{\mathbf{q}+\mathbf{G}} = \sum_{\mathbf{k}, \mathbf{G}', X, \eta, s} \left( c_{\mathbf{k}, \mathbf{G}', X, \eta, s}^\dagger c_{\mathbf{k}+\mathbf{q}+\mathbf{G}, \mathbf{G}', X, \eta, s} - \frac{\nu+4}{8} \delta_{\mathbf{q}, 0} \delta_{\mathbf{G}, 0} \right). \quad (5)$$

Here  $\delta\rho_{\mathbf{q}}$  is the electron density operator with the reference to  $(\nu+4)/8$ , where  $\nu$  is the filling parameter with  $\nu=0$  as charge neutrality.  $V(\mathbf{q})$  is the long-range Coulombic interaction, decaying as  $V(\mathbf{q}) = \frac{e^2}{2\varepsilon} \frac{1}{|\mathbf{q}|} (1 - e^{-|\mathbf{q}|d})$  [37], where  $d/2$  is the distance between TBG and a single gate (bottom gate) [57] (here we set  $d=40$  nm) and  $\varepsilon=7\varepsilon_0$  is the dielectric constant.  $X$  is the index referring to layers and sublattices, as  $X \in \{A_1, B_1, A_2, B_2\}$ . The fermion momentum transfer  $\mathbf{q}+\mathbf{G}$  is cut off at the amplitude of  $|\mathbf{G}_1|$ .  $\Omega = N_k |\mathbf{a}_{M1}| |\mathbf{a}_{M2}| \sqrt{3}/2$  is the total area of morié superlattice that we consider in real space, where  $N_k = L \times L$  is the number of  $\mathbf{k}$  points sampling in mBZ and  $L$  is the linear size.

As shown in Fig. S2 of SM [56], even in non-chiral cases ( $u_0 > 0$ ), the lowest two bands of  $H_0$  are still flat and isolated from the remote bands, except when  $u_0 \approx u_1$  ( $u_0 = 100, 110, 120$  meV) or  $u_0 > 150$  meV. In these isolated flat-band cases, therefore, the low energy physics of  $H = H_0 + H_1$  can be well captured by the two flat bands, which also means  $H$  can be projected to the flat bands. The eigenvalues and eigenvectors of  $H^{\eta, s}(\mathbf{k})$  are  $\epsilon_m^{\eta, s}(\mathbf{k})$  and  $|u_{\mathbf{k}, m, \eta, s}\rangle$ , where  $m = \pm$  is the indice for the flat bands. Projecting  $H$  into the flat bands, as  $c_{\mathbf{k}, m, \eta, s}^\dagger = \sum_{\mathbf{G}, X} c_{\mathbf{k}, \mathbf{G}, X, \eta, s}^\dagger |u_{\mathbf{k}, m, \eta, s}\rangle_{\mathbf{G}, X}$ , yields

$$\begin{aligned} H_0 &= \sum_{\mathbf{k}, m, \eta, s} \epsilon_m^{\eta, s}(\mathbf{k}) c_{\mathbf{k}, m, \eta, s}^\dagger c_{\mathbf{k}, m, \eta, s}, \\ H_1 &= \frac{1}{2\Omega} \sum_{|\mathbf{q}+\mathbf{G}| \neq 0} V(\mathbf{q}+\mathbf{G}) \delta\rho_{\mathbf{q}+\mathbf{G}} \delta\rho_{-\mathbf{q}-\mathbf{G}}, \end{aligned} \quad (6)$$

where  $\delta\rho_{\mathbf{q}+\mathbf{G}} = \sum_{\mathbf{k}, m_1, m_2, \eta, s} \lambda_{m_1, m_2, \eta, s}(\mathbf{k}, \mathbf{k}+\mathbf{q}+\mathbf{G}) \left( d_{\mathbf{k}, m_1, \eta, s}^\dagger d_{\mathbf{k}+\mathbf{q}+\mathbf{G}, m_2, \eta, s} - \frac{\nu+4}{8} \delta_{\mathbf{q}, 0} \delta_{m_1, m_2} \right)$ , and the form factor  $\lambda_{m_1, m_2, \eta, s}(\mathbf{k}, \mathbf{k}+\mathbf{q}+\mathbf{G}) \equiv \langle u_{\mathbf{k}, m_1, \eta, s} | u_{\mathbf{k}+\mathbf{q}+\mathbf{G}, m_2, \eta, s} \rangle$ . To efficiently simulate the system at filling  $\nu = -3$ , same as earlier studies [32, 33], we take the two flat bands in  $\eta = +$  valley with spin up  $\uparrow$  and set the flat bands to be half filled. It is feasible due to that the ground state at this filling is expected to be spin and valley polarized, while other flat bands, which remain empty, can be safely ignored in the simulations.

Due to the flatness of lowest energy bands, as shown in Fig. S2,  $H_0$  can be ignored in our simulations. The partition function thus reads  $Z = \text{Tr}(e^{-\beta H_1})$ , where  $\beta = 1/k_B T$  and  $T$  is the temperature. Details of momentum-space QMC implementation are given in SM [56]. The QMC simulations of Eq. (6) are sign-problematic, as shown in Fig. S3, where the average sign,  $\langle \text{sign} \rangle$ , reaches 0 at around 1 meV when  $u_0 \geq 40$  meV. Nevertheless, our stable and reproducible results show that a QMC simulation can still be efficiently and reliably done when  $\langle \text{sign} \rangle > 0.05$  with reasonable computing resources. In addition, a *sign bound theory* proves that, at integer fillings, the  $\langle \text{sign} \rangle$  of the TBG system has a lower bound depending polynomially on the system size ( $N_k$ ) [58, 59], differing from the

conventional exponential decay of  $\langle \text{sign} \rangle \sim e^{-\beta N_k}$ . The sign bound greatly reduces the computational complexity of correlated flat-band systems [38] such as the present case. With the reliable imaginary time Green's function, we further employ the stochastic analytic continuation (SAC) [35, 37, 60–63] method to extract the real frequency spectra, as will be shown below. ED is also implemented to benchmark the single-particle gaps, as shown in Fig. S6.

**Results.**— The ground state of this system at chiral limit was found to be a Chern number polarized QAH state as shown in Fig. 1 and Fig. 2 (see data of  $u_0 = 0$ ), being consistent to our previous study [37]. To investigate if the QAH state sustains in realistic cases, the correlation function of the QAH order is calculated when the system is away from chiral limit. A perturbation term (see SM [56]),  $\delta\sigma_z$ , with  $\delta = 1$  meV and  $\sigma_z$  the third Pauli matrix, is added to the bottom layer of  $H_0$  to obtain a well-defined Chern basis. Please note that this perturbation term plays the role of hexagonal boron nitride in a bottom gated experiment [64], which breaks  $C_2\mathcal{T}$  but  $\mathcal{T}$ , meaning the time-reversal symmetry can still be spontaneously broken. The QAH order parameter is defined as  $P_C/N_k$ , where  $P_C = N_+ - N_-$  and  $N_m = \sum_{\mathbf{k}} c_{\mathbf{k}, m}^\dagger c_{\mathbf{k}, m}$ , the occupation number operator of two flat bands which have  $\pm$  Chern numbers each. The correlation function of this QAH order, or Chern number polarization, is  $S \equiv \langle (N_+ - N_-)^2 \rangle / N_k^2$ . Its  $T$  and  $u_0$  dependence for  $L = 4$  system is shown in Fig. 2. For specific  $u_0$ ,  $S$  increases with decreasing  $T$ , which manifests spontaneous time-reversal symmetry breaking and a QAH state (a topological Mott insulator) at low temperature [37, 65, 66]. However, with fixed and low  $T$ ,  $S$  reduces when  $u_0$  increases, indicating a phase transition from the QAH state to another phase (a heavy-fermion semimetal as will be shown later). For each fixed  $u_0$ , finite-size scaling is carried out to derive the critical temperature ( $T_c$ ) of the spontaneous time-reversal symmetry breaking of the QAH state, as shown in Fig. S7, where the 2D Ising exponents  $\beta = 1/8$  and  $\nu = 1$  for the scaling form  $S(T, L) L^{2\beta/\nu} = f((T - T_c) L^{1/\nu})$ , with  $f$  being the scaling function, are used. The obtained  $T_c$  reduces with increasing  $u_0$ , as shown in Fig. 1 (a), and it can be deduced that, at  $u_0 \sim 80$  meV,  $T_c$  is zero within our resolution.

Such vanishing of the QAH phase as a function of  $u_0$  is consistent with the evolution of the system's gap, single-particle gap ( $\Delta$ ) of  $\Gamma$  point, with different system size  $L$ , as shown in Fig. 1 (b). Since it is least as proved by Fig. S5,  $\Delta(\Gamma)$  can be treated as the system's gap. The value of  $\Delta(\Gamma)$  is obtained by fitting imaginary time ( $\tau$ ) Green's functions (GFs) to a range with linear  $\tau$ -dependence of logarithmic GFs, see Figs. S4 and S5 in SM [56]. It is apparently in Fig. 1 (b) that, with enlarging system sizes, the system's gap closes at around  $u_0 = 80$  meV, while gaps of other  $\mathbf{k}$  points of mBZ remain finite and significant even for large  $u_0$ , as shown in Fig. S5 in SM [56], implying a semi-metallic state. It is found as well that  $T_c$ -s in Fig. 1 (a) are much smaller than the system's gap in Fig. 1 (b), due to particle-hole excitons with smaller gaps compared to those of single particle in the QAH phase, which has been evidenced in our previous works [37, 66].

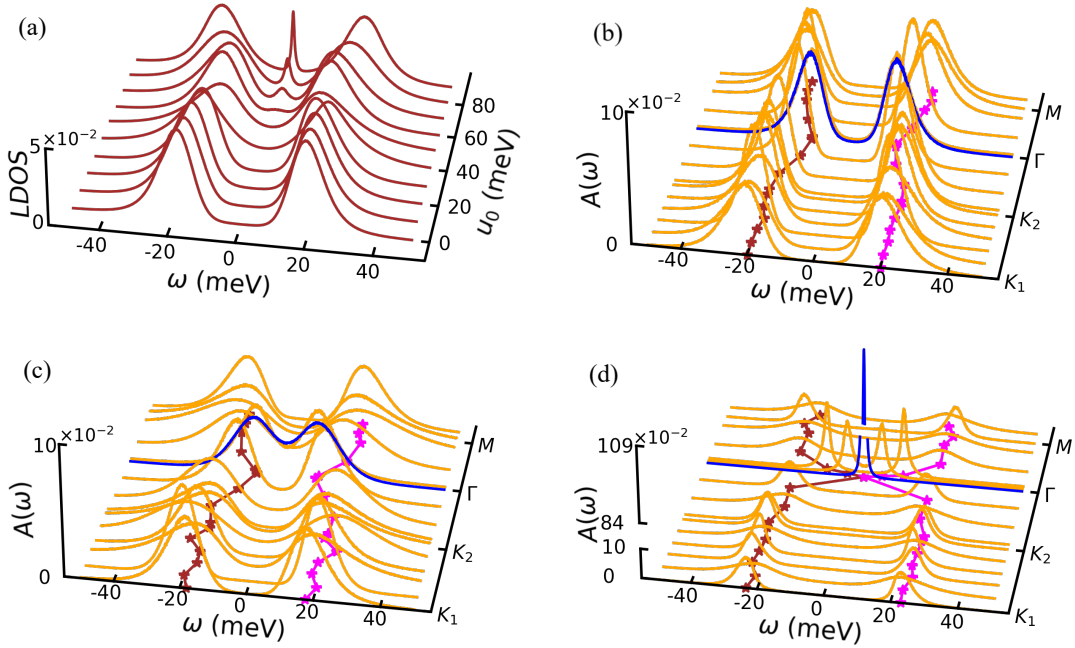


FIG. 3. **LDOS and single-particle spectra.** (a) Normalized local density of states (*LDOS*) versus energy  $\omega$  and  $u_0$ . (b), (c), and (d) Single-particle spectra  $A(\mathbf{k}, \omega)$  along a high-symmetry path when  $u_0 = 0$ ,  $u_0 = 40$  meV, and  $u_0 = 90$  meV, respectively, where the star-lines represent the positions of the spectra peaks. Please note that the vertical axis in (d) is broken, due to the sharp peak of  $\Gamma$ , to make the drawing compact. Here we show the spectra of  $L = 5$  with shifted boundary to increase momentum resolution, and the blue lines denote the spectra of  $\Gamma$ , while the orange lines are  $A(\mathbf{k}, \omega)$  of other momentum points.

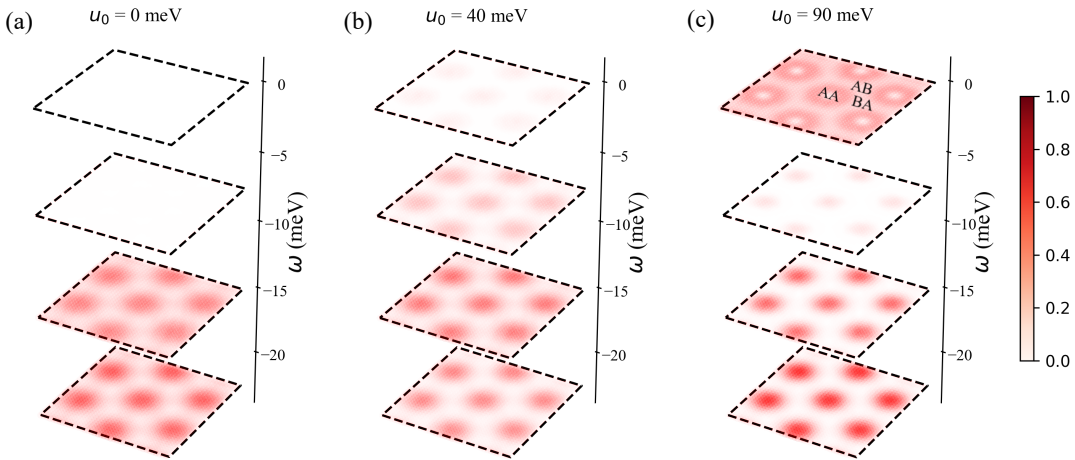


FIG. 4. **Real-space spectra  $A(r, \omega)$  at various  $u_0$  and  $\omega$ .** Here  $u_0$  equals to (a) 0 meV, (b) 40 meV, and (c) 90 meV, while  $\omega$  is chosen to be 0, 7.5, 15, and 22.5 meV in each figure. The intensity of red stands for the value of  $A(r, \omega)$ , with a color bar locating at the right of (c). Positions of AA-, AB-, and BA-stacking areas are labeled in (c).

To further reveal the evolution from QAH to a semimetal state with increasing  $u_0$ , we derive the single-particle spectra,  $A(\mathbf{k}, \omega)$ , and the local density of state,  $LDOS = \sum_{\mathbf{k}} A(\mathbf{k}, \omega) / N_{\mathbf{k}}$ , from QMC-SAC scheme, as shown in Fig. 3. As consistent to  $T_c$  and  $\Delta$  in the QAH phase,  $A(\mathbf{k}, \omega)$  is gapped for all  $\mathbf{k}$ -points, though the gap of  $A(\Gamma, \omega)$  is the least and gradually decreases with growing  $u_0$  (Fig. 3 (b) (c)) and totally closes when  $u_0 = 90$  meV (Fig. 3 (d)). In addition, the

positions of peaks are drawn in Fig. 3 (b)-(d), making energy dispersion with interaction (interactive dispersion) of different  $u_0$ . The *LDOS* remains gapped except a peak around Fermi level arises when  $u_0 \geq 60$  meV (Fig. 3 (a)). This peak comes from the closing of  $\Delta(\Gamma)$ , as demonstrated in Fig. 3 (d), while the spectra of other  $\mathbf{k}$ -points remain well gapped. The confirmation of the semimetal state is that the peak of *LDOS* at Fermi level (when  $u_0 = 90$  meV) reduces to a minimum

but finite value as the system size enlarges, as shown in Fig. S8. This minimum value indicates the phase is probably a quadratic band touching semimetal, which is also verified by the interactive dispersion as shown in Fig. S9. Therefore, the magic-angle TBG system is expected to be a quadratic band touching semimetal when  $\nu = -3$  and  $u_0 \geq 80$  meV. It is so experimentally and realistically.

The closing of the system's gap at  $\Gamma$  is consistent with the recently proposed heavy-fermion picture of magic-angle TBG [31, 50–55]. In the heavy-fermion representation, the flat band is mostly composed of localized electrons, except for the tiny vicinity of  $\Gamma$ , which is mainly contributed by delocalized electronic states. In the flat band limit, strong interactions between localized electrons ought to induce an energy gap in single-particle spectra. However, this interaction induced gap is expected to be much smaller in the narrow surrounding of  $\Gamma$ , since the fermion states there are delocalized with weaker interaction, and it is indeed so at chiral limit and when  $u_0 = 40$  meV, as shown in Fig. 3 (b) and (c)]. Moreover, the interactions among fermions around  $\Gamma$  can be further weaker as the system deviates from chiral limit (increasing  $u_0$ ), and the corresponding gaps decline and eventually close when  $u_0$  goes beyond a threshold value ( $u_0 \sim 80$  meV), as illustrated by Fig. 3 (d).

To further scrutinize the heavy-fermion character of the semimetal phase, here we directly probe the localized and delocalized electron states via real space spectra by projecting  $A(\mathbf{k}, \omega)$  with the real space wavefunction ( $\psi_{\mathbf{k}}(\mathbf{r}, X)$ ) of  $H_0$ ,  $A(r, \omega) = \sum_{\mathbf{k}, X} \psi_{\mathbf{k}}^\dagger(\mathbf{r}, X) A(\mathbf{k}, \omega) \psi_{\mathbf{k}}(\mathbf{r}, X)$ , as a function of  $u_0$  and shown in Fig. 4. It can be clearly seen that the density of low energy electrons ( $\omega = 0$  meV, first row of panels (a) - (c)) increases in AB/BA stacking regions (or be lifted as the maximum values are around AA stacking center, where however the minimum values locate), marking the emergence of the semi-metallic state. Meanwhile, the localized electrons ( $\omega = 15, 22.5$  meV, bottom two rows of panels (a) - (c)) always and further concentrate at AA centers as  $u_0$  grows, which is consistent with the heavy-fermion picture [50, 51] and experiments [8, 9]. Furthermore, the density of electrons with intermediate energy ( $\omega = 7.5$  meV, second row in panel (c)) manifests a minimum value, separating the itinerant and localized electrons when  $u_0 = 90$  meV. These observations confirm that the realistic magic-angle TBG of  $\nu = -3$  can truly be viewed as a heavy-fermion system. Besides, the itinerant electrons of  $A(r, \omega = 0)$  in panel (c) come from  $A(\Gamma, \omega = 0)$  in Fig. 3 (d).

**Discussions.**— In this study, an evolution from Chern insulator to heavy-fermion semimetal is found for  $\nu = -3$  (or  $\nu = 3$  considering particle-hole symmetry) filling magic-angle TBG by varying AA hopping strength,  $u_0$ , which can be experimentally altered. The transition happens at  $u_0 \approx 0.7u_1$ , where the Chern number polarization vanishes and a peak in LDOS at Fermi level emerges. The intensity of this peak rises as  $u_0$  increases for a specific system size, and reduces to a minimum but finite value as  $L$  enlarges for a specific  $u_0$ , which manifests a correlated semimetal state. The momentum and real-space distributions of the localized electrons are well separated from

those of itinerant electrons. The nature of the found semimetal state implies that magic-angle TBG can be treated as a heavy-fermion system at least for  $\nu = -3$ , whose itinerant electrons are of  $\Gamma$  point. It is also noted that, at the present integer filling, CDW or  $s$ -wave superconductivity is not detected in the semi-metallic state (see Sec. VI of SM [56]). Our findings shed new light on the correlated nature of TBG and provide critical information for understanding this fascinating system.

*Acknowledgments* — We thank DongKeun Ki and Wang Yao for useful discussions. CH, XZ, GPP and ZYM acknowledge the support from the Research Grants Council (RGC) of Hong Kong SAR of China (Project Nos. 17301420, 17301721, AoE/P-701/20, 17309822, HKU C7037-22G), the ANR/RGC Joint Research Scheme sponsored by RGC of Hong Kong and French National Research Agency (Project No. A\_HKU703/22), the Strategic Priority Research Program of Chinese Academy of Sciences (Grant No. XDB33000000), and K. C. Wong Education Foundation (Grant No. GJTD-2020-01). We thank the HPC2021 system of Information Technology Services and the Blackbody HPC system at the Department of Physics of the University of Hong Kong for providing computational resources that have contributed to the research results in this paper.

---

\* sunkai@umich.edu

† daix@ust.hk

‡ zymeng@hku.hk

- [1] G. Trambly de Laissardière, D. Mayou, and L. Magaud, *Nano Letters* **10**, 804 (2010).
- [2] G. Trambly de Laissardière, D. Mayou, and L. Magaud, *Phys. Rev. B* **86**, 125413 (2012).
- [3] R. Bistritzer and A. H. MacDonald, *Proceedings of the National Academy of Sciences* **108**, 12233 (2011).
- [4] Y. Cao, V. Fatemi, A. Demir, S. Fang, S. L. Tomarken, J. Y. Luo, J. D. Sanchez-Yamagishi, K. Watanabe, T. Taniguchi, E. Kaxiras, *et al.*, *Nature* **556**, 80 (2018).
- [5] Y. Cao, D. Rodan-Legrain, O. Rubies-Bigorda, J. M. Park, K. Watanabe, T. Taniguchi, and P. Jarillo-Herrero, *Nature* **583**, 215 (2020).
- [6] H. Polshyn, M. Yankowitz, S. Chen, Y. Zhang, K. Watanabe, T. Taniguchi, C. R. Dean, and A. F. Young, *Nature Physics* **15**, 1011 (2019).
- [7] X. Liu, Z. Wang, K. Watanabe, T. Taniguchi, O. Vafek, and J. Li, *Science* **371**, 1261 (2021).
- [8] Y. Xie, B. Lian, B. Jäck, X. Liu, C.-L. Chiu, K. Watanabe, T. Taniguchi, B. A. Bernevig, and A. Yazdani, *Nature* **572**, 101 (2019).
- [9] Y. Choi, J. Kemmer, Y. Peng, A. Thomson, H. Arora, R. Polski, Y. Zhang, H. Ren, J. Alicea, G. Refael, *et al.*, *Nature physics* **15**, 1174 (2019).
- [10] K. P. Nuckolls, M. Oh, D. Wong, B. Lian, K. Watanabe, T. Taniguchi, B. A. Bernevig, and A. Yazdani, *Nature* **588**, 610 (2020).
- [11] Y. Saito, J. Ge, L. Rademaker, K. Watanabe, T. Taniguchi, D. A. Abanin, and A. F. Young, *Nature Physics* **17**, 478 (2021).
- [12] I. Das, X. Lu, J. Herzog-Arbeitman, Z.-D. Song, K. Watanabe, T. Taniguchi, B. A. Bernevig, and D. K. Efetov, *Nature Physics*

- 17, 710 (2021).
- [13] S. Wu, Z. Zhang, K. Watanabe, T. Taniguchi, and E. Y. Andrei, *Nature materials* **20**, 488 (2021).
- [14] P. Potasz, M. Xie, and A. H. MacDonald, *Phys. Rev. Lett.* **127**, 147203 (2021).
- [15] A. Jaoui, I. Das, G. Di Battista, J. Díez-Mérida, X. Lu, K. Watanabe, T. Taniguchi, H. Ishizuka, L. Levitov, and D. K. Efetov, *Nature Physics* **18**, 633 (2022).
- [16] Y. Cao, V. Fatemi, S. Fang, K. Watanabe, T. Taniguchi, E. Kaxiras, and P. Jarillo-Herrero, *Nature* **556**, 43 (2018).
- [17] Y. Cao, D. Rodan-Legrain, J. M. Park, N. F. Yuan, K. Watanabe, T. Taniguchi, R. M. Fernandes, L. Fu, and P. Jarillo-Herrero, *science* **372**, 264 (2021).
- [18] M. Yankowitz, S. Chen, H. Polshyn, Y. Zhang, K. Watanabe, T. Taniguchi, D. Graf, A. F. Young, and C. R. Dean, *Science* **363**, 1059 (2019).
- [19] J. Díez-Merida, A. Díez-Carlón, S. Yang, Y.-M. Xie, X.-J. Gao, K. Watanabe, T. Taniguchi, X. Lu, K. T. Law, and D. K. Efetov, *arXiv preprint arXiv:2110.01067* (2021).
- [20] G. Di Battista, P. Seifert, K. Watanabe, T. Taniguchi, K. C. Fong, A. Principi, and D. K. Efetov, *Nano Letters* **22**, 6465 (2022).
- [21] B. Lian, Z.-D. Song, N. Regnault, D. K. Efetov, A. Yazdani, and B. A. Bernevig, *Phys. Rev. B* **103**, 205414 (2021).
- [22] F. Xie, A. Cowsik, Z.-D. Song, B. Lian, B. A. Bernevig, and N. Regnault, *Phys. Rev. B* **103**, 205416 (2021).
- [23] N. Bultinck, E. Khalaf, S. Liu, S. Chatterjee, A. Vishwanath, and M. P. Zaletel, *Phys. Rev. X* **10**, 031034 (2020).
- [24] P. Wilhelm, T. C. Lang, and A. M. Läuchli, *Phys. Rev. B* **103**, 125406 (2021).
- [25] Y. Zhang, K. Jiang, Z. Wang, and F. Zhang, *Phys. Rev. B* **102**, 035136 (2020).
- [26] J. Liu and X. Dai, *Phys. Rev. B* **103**, 035427 (2021).
- [27] K. Hejazi, X. Chen, and L. Balents, *Phys. Rev. Res.* **3**, 013242 (2021).
- [28] F. Xie, J. Kang, B. A. Bernevig, O. Vafek, and N. Regnault, *Phys. Rev. B* **107**, 075156 (2023).
- [29] X. Lin and J. Ni, *Phys. Rev. B* **102**, 035441 (2020).
- [30] Y. H. Kwan, G. Wagner, N. Chakraborty, S. H. Simon, and S. A. Parameswaran, *Phys. Rev. B* **104**, 115404 (2021).
- [31] A. Datta, M. J. Calderón, A. Camjayi, and E. Bascones, *arXiv e-prints*, *arXiv:2301.13024* (2023), *arXiv:2301.13024* [cond-mat.str-el].
- [32] J. Kang and O. Vafek, *Phys. Rev. B* **102**, 035161 (2020).
- [33] T. Soejima, D. E. Parker, N. Bultinck, J. Hauschild, and M. P. Zaletel, *Phys. Rev. B* **102**, 205111 (2020).
- [34] X. Zhang, G. Pan, Y. Zhang, J. Kang, and Z. Y. Meng, *Chinese Physics Letters* **38**, 077305 (2021).
- [35] G. Pan, X. Zhang, H. Li, K. Sun, and Z. Y. Meng, *Phys. Rev. B* **105**, L121110 (2022).
- [36] J. S. Hofmann, E. Khalaf, A. Vishwanath, E. Berg, and J. Y. Lee, *Phys. Rev. X* **12**, 011061 (2022).
- [37] G. Pan, X. Zhang, H. Lu, H. Li, B.-B. Chen, K. Sun, and Z. Y. Meng, *Phys. Rev. Lett.* **130**, 016401 (2023).
- [38] X. Zhang, G. Pan, B.-B. Chen, H. Li, K. Sun, and Z. Y. Meng, *arXiv e-prints*, *arXiv:2210.11733* (2022), *arXiv:2210.11733* [cond-mat.str-el].
- [39] Y. Saito, J. Ge, K. Watanabe, T. Taniguchi, and A. F. Young, *Nature Physics* **16**, 926 (2020).
- [40] X. Lu, P. Stepanov, W. Yang, M. Xie, M. A. Aamir, I. Das, C. Urgell, K. Watanabe, T. Taniguchi, G. Zhang, *et al.*, *Nature* **574**, 653 (2019).
- [41] P. Stepanov, I. Das, X. Lu, A. Fahimniya, K. Watanabe, T. Taniguchi, F. H. Koppens, J. Lischner, L. Levitov, and D. K. Efetov, *Nature* **583**, 375 (2020).
- [42] A. B. Kuzmenko, I. Crassee, D. van der Marel, P. Blake, and K. S. Novoselov, *Phys. Rev. B* **80**, 165406 (2009).
- [43] E. Y. Andrei and A. H. MacDonald, *Nature materials* **19**, 1265 (2020).
- [44] Y. Xu, S. Liu, D. A. Rhodes, K. Watanabe, T. Taniguchi, J. Hone, V. Elser, K. F. Mak, and J. Shan, *Nature* **587**, 214 (2020).
- [45] Y. Xie, B. Lian, B. Jäck, X. Liu, C.-L. Chiu, K. Watanabe, T. Taniguchi, B. A. Bernevig, and A. Yazdani, *Nature* **572**, 101 (2019).
- [46] N. N. T. Nam and M. Koshino, *Phys. Rev. B* **96**, 075311 (2017).
- [47] M. Koshino, N. F. Q. Yuan, T. Koretsune, M. Ochi, K. Kuroki, and L. Fu, *Phys. Rev. X* **8**, 031087 (2018).
- [48] D. Xi, *Chinese Physics Letters* **39**, 50101 (2022).
- [49] H. Li, U. Kumar, K. Sun, and S.-Z. Lin, *Phys. Rev. Research* **3**, L032070 (2021).
- [50] Z.-D. Song and B. A. Bernevig, *Phys. Rev. Lett.* **129**, 047601 (2022).
- [51] H. Shi and X. Dai, *Phys. Rev. B* **106**, 245129 (2022).
- [52] D. Călugăru, M. Borovkov, L. L. Lau, P. Coleman, Z.-D. Song, and B. A. Bernevig, *arXiv preprint arXiv:2303.03429* (2023).
- [53] H. Hu, B. A. Bernevig, and A. M. Tsvelik, *arXiv preprint arXiv:2301.04669* (2023).
- [54] H. Hu, G. Rai, L. Crippa, J. Herzog-Arbeitman, D. Călugăru, T. Wehling, G. Sangiovanni, R. Valenti, A. M. Tsvelik, and B. A. Bernevig, *arXiv preprint arXiv:2301.04673* (2023).
- [55] Y.-Z. Chou and S. D. Sarma, *arXiv preprint arXiv:2211.15682* (2022).
- [56] The detailed real space TBG lattice and its Brillouin zone, the analyses of the sign problem and results of various physical observables are given in this Supplemental Material.
- [57] S. Liu, E. Khalaf, J. Y. Lee, and A. Vishwanath, *Phys. Rev. Research* **3**, 013033 (2021).
- [58] X. Zhang, G. Pan, X. Y. Xu, and Z. Y. Meng, *Phys. Rev. B* **106**, 035121 (2022).
- [59] G. Pan and Z. Y. Meng, *arXiv preprint arXiv:2204.08777* (2022).
- [60] Z. Yan and Z. Y. Meng, *arXiv e-prints*, *arXiv:2112.05886* (2021), *arXiv:2112.05886* [cond-mat.str-el].
- [61] X. Zhang, K. Sun, H. Li, G. Pan, and Z. Y. Meng, *Phys. Rev. B* **106**, 184517 (2022).
- [62] C. Zhou, Z. Yan, H.-Q. Wu, K. Sun, O. A. Starykh, and Z. Y. Meng, *Phys. Rev. Lett.* **126**, 227201 (2021).
- [63] Z. Yan, Y.-C. Wang, N. Ma, Y. Qi, and Z. Y. Meng, *npj Quantum Materials* **6**, 39 (2021).
- [64] F. Guinea, M. I. Katsnelson, and A. Geim, *Nature Physics* **6**, 30 (2010).
- [65] B.-B. Chen, Y. D. Liao, Z. Chen, O. Vafek, J. Kang, W. Li, and Z. Y. Meng, *Nature Communications* **12**, 5480 (2021).
- [66] X. Lin, B.-B. Chen, W. Li, Z. Y. Meng, and T. Shi, *Phys. Rev. Lett.* **128**, 157201 (2022).

## SUPPLEMENTARY MATERIALS

In this Supplementary Material, we introduce the real space morié lattice and its single-particle dispersion, propose the validation of projecting  $H$  into flat bands in Sec. I, and elucidate the implementation of the momentum-space QMC method and the sign problem of magic-angle TBG system when  $\nu = -3$  in Sec. II. In Sec. III, The decaying of imaginary Green's functions and the derived gaps, with the comparison to those from ED, are shown. In Sec. IV, the obtaining of a well defined Chern basis and the determination of the critical temperature of QAH state by finite-size scaling are illustrated. The semi-metallic state is varified by checking the convergence of Green's functions, the reducing of peak intensity in spectra, as well as the interactive dispersion with enlarging system size in Sec. V. Finally, the absence of CDW or s-wave superconductivity is presented in Sec. VI, and the implementation of ED is elucidated in Sec. VII.

### I. Morié lattice and single-particle dispersions

The real space morié lattice generated by twisted bilayer graphene is shown in Fig. S1, where a morié unit cell (mUC) and the corresponding riciprocal first Brillouin zone, which is dubbed as morié Brillouin zone (mBZ), are drawn. The interlayer hopping strategies are also shown in the right panel.

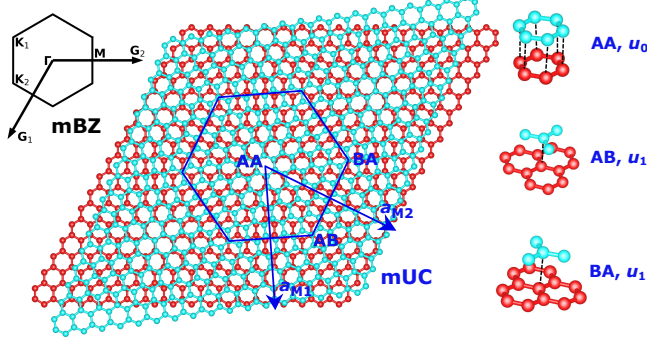


FIG. S1. Morié unit cell (mUC, blue hexagon) and its Brillouin zone (mBZ, black hexagon), as well as three kinds of stackings and hoppings (AA, AB, and BA) of TBG.  $u_0$  and  $u_1$  are hopping strengths of AA- and AB/BA-stacking areas, respectively. The top (bottom) layer of TBG are denoted by cyan (red) color.  $\{\mathbf{a}_{M1}, \mathbf{a}_{M2}\}$  and  $\{\mathbf{G}_1, \mathbf{G}_2\}$  are the primitive lattice vectors of mUC and mBZ, respectively.  $\Gamma$  is the origin of mBZ, and  $\mathbf{K}_1$  and  $\mathbf{K}_2$  are the two Dirac points of the same vally and different layers (1,2). The twisted angle  $\theta$  in this schematic is  $10^\circ$ , while that of the case we investigate in the main text is  $1.08^\circ$ .

From this morié lattice, a momentum space single-particle Hamiltonian,  $H_0$ , considering intralayer hopping and interlayer hopping, can be constructed, as described in the main text. The dispersions of  $H_0$  with different  $u_0$  are shown in Fig. S2, where two low energy bands are quite flat and isolated from remote bands when  $u_0 \leq 90$  meV. It implies that the low

energy physics can be well captured by these two bands. The projection of  $H$  to flat bands, as depicted in the main text, makes the description of  $H$  easier since only two bands are considered. However, we suppose that the projections when  $u_0 = 110$  (meV) and  $u_0 > 150$  (meV) fail as remote bands are too close to flat bands.

### II. Implementation of momentum space QMC method and the sign problem

The partition function can be Trotter-decoupled after splitting inverse temperature into  $N_\tau$  pieces,  $\beta = \Delta\tau N_\tau$ , with an error of order  $\Delta\tau^2$ . That is

$$\begin{aligned} Z &= \text{Tr} \left( e^{-\beta H} \right) \\ &= \text{Tr} \left( \left( e^{-\Delta\tau H} \right)^{N_\tau} \right) \\ &= \text{Tr} \left( \prod_{\tau=\Delta\tau}^{\beta} e^{-\Delta\tau H_0} e^{-\Delta\tau H_1} \right) + \mathcal{O}(\Delta\tau^2). \end{aligned} \quad (7)$$

Denoting  $\mathbf{Q} = \mathbf{q} + \mathbf{G}$ ,  $H_1$  can be rewritten as

$$\begin{aligned} H_1 &= \sum_{|\mathbf{Q}| \neq 0} \frac{1}{2\Omega} V(\mathbf{Q}) \delta\rho_{\mathbf{Q}} \delta\rho_{-\mathbf{Q}} \\ &= \sum_{|\mathbf{Q}| \neq 0} \frac{1}{8\Omega} V(\mathbf{Q}) \left( (\delta\rho_{-\mathbf{Q}} + \delta\rho_{\mathbf{Q}})^2 - (\delta\rho_{-\mathbf{Q}} - \delta\rho_{\mathbf{Q}})^2 \right), \end{aligned} \quad (8)$$

where an approximation,  $[\delta\rho_{-\mathbf{Q}}, \delta\rho_{\mathbf{Q}}] \approx 0$ , is applied [34]. Thus,  $e^{-\Delta\tau H_1}$  can be further decoupled to an auxiliary field by the Hubbard-Stratonovich transformation, with an error of order  $\Delta\tau^4$ , as

$$\begin{aligned} e^{-\Delta\tau H_1} &= \prod_{|\mathbf{Q}| \neq 0} \frac{1}{16} \sum_{l_1\mathbf{Q}, l_2\mathbf{Q}} \gamma(l_1\mathbf{Q}) \gamma(l_2\mathbf{Q}) e^{i\sqrt{\alpha}\eta(l_1\mathbf{Q})(\delta\rho_{-\mathbf{Q}} + \delta\rho_{\mathbf{Q}})} e^{\sqrt{\alpha}\eta(l_2\mathbf{Q})(\delta\rho_{-\mathbf{Q}} - \delta\rho_{\mathbf{Q}})} \\ &+ \mathcal{O}(\Delta\tau^4), \end{aligned} \quad (9)$$

where  $l = \pm 1, \pm 2$ , is the auxiliary field, and  $\gamma(\pm 1) = 1 + \sqrt{6}/3$ ,  $\gamma(\pm 2) = 1 - \sqrt{6}/3$ ,  $\eta(\pm 1) = \pm\sqrt{6 - 2\sqrt{6}}$ , and  $\eta(\pm 2) = \pm\sqrt{6 + 2\sqrt{6}}$ .  $\alpha = \Delta\tau V(\mathbf{q})/8\Omega$ .

The partition function can be finally written as  $Z = \sum_{l_{\tau 1\mathbf{Q}}, l_{\tau 2\mathbf{Q}}} \text{Tr} U_C$ , with

$$\begin{aligned} U_C &= \prod_{\tau=\Delta\tau}^{\beta} e^{-\Delta\tau H_0} \prod_{|\mathbf{Q}| \neq 0} \\ &\frac{1}{16} \gamma(l_{\tau 1\mathbf{Q}}) \gamma(l_{\tau 2\mathbf{Q}}) e^{i\sqrt{\alpha}\eta(l_{\tau 1\mathbf{Q}})(\delta\rho_{-\mathbf{Q}} + \delta\rho_{\mathbf{Q}})} e^{\sqrt{\alpha}\eta(l_{\tau 2\mathbf{Q}})(\delta\rho_{-\mathbf{Q}} - \delta\rho_{\mathbf{Q}})}, \end{aligned} \quad (10)$$

a configuration of  $\{l_{\tau 1\mathbf{Q}}, l_{\tau 2\mathbf{Q}}\}$  labeled by  $C$ . Physical quantities,  $O$ , can thus be obtained by sampling the auxiliary field,

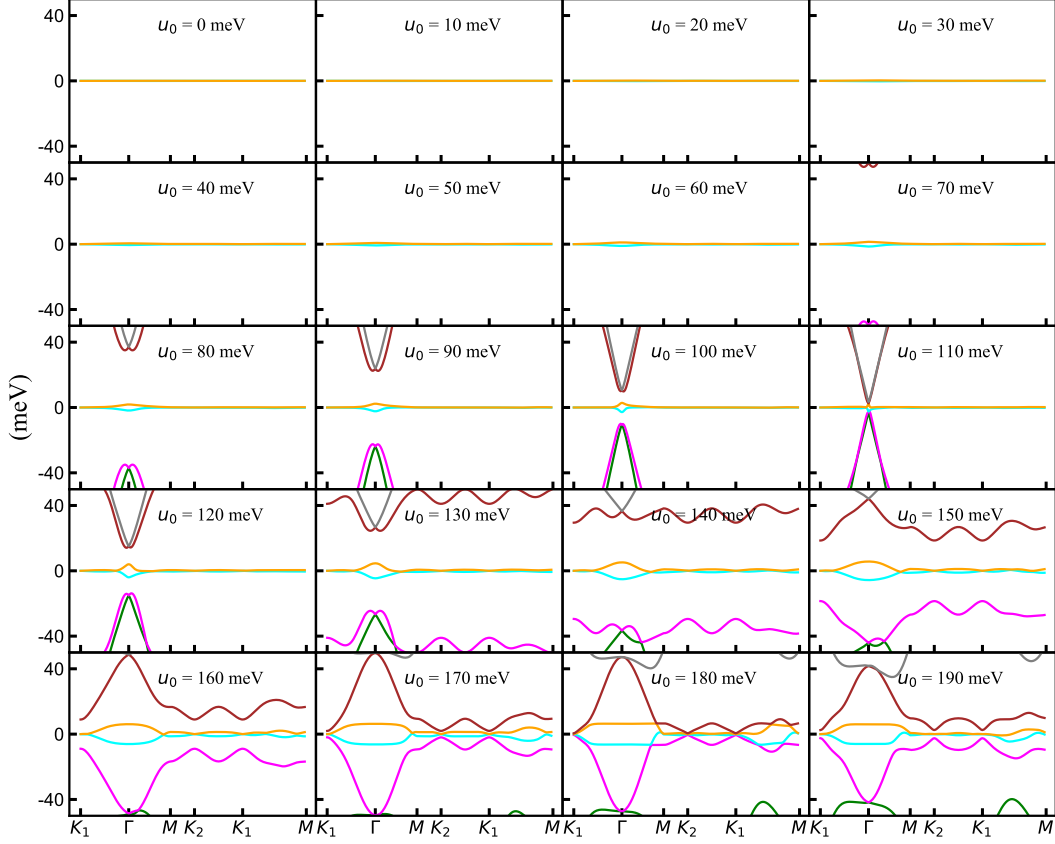


FIG. S2. Single-particle dispersions of  $H_0$  along the high-symmetry line. The remote bands are beyond the scale when  $u_0 < 70$  meV, and approaches the flat bands around  $\Gamma$  point as  $u_0$  further increases. Note that the lowest remote bands touch the flat bands at  $\Gamma$  point only when  $u_0 = 110$  meV ( $u_0 = u_1$ ). The band width of the flat bands enlarge as  $u_0$  increases, but remains a quite small value (less than 5 meV when  $u_0 = 90$  meV).

as

$$\begin{aligned}
 \langle O \rangle &= \frac{\text{Tr}(e^{-\beta H} O)}{Z} \\
 &= \sum_C \frac{\text{Tr}(U_C O)}{Z} \\
 &= \sum_C \frac{\text{Tr}(U_C)}{Z} \frac{\text{Tr}(U_C O)}{\text{Tr}(U_C)},
 \end{aligned} \tag{11}$$

with  $\text{Tr}(U_C)/Z$  or  $\text{Tr}(U_C)$  being the sampling weight and being denoted as  $P_C$ .

However,  $P_C$  of the magic-angle TBG with  $\nu = -3$  is not constantly positive, which is narrated to be sign-problematic. Nevertheless, the symmetries make  $P_C$  real [34] and the average of its sign,  $\langle \text{sign} \rangle = \sum_C \text{sgn}(P_C)$ , is always positive and ranges from 0 to 1. Here 1 means no sign problem while 0 means the simulation is meaningless. The belief populates that  $\langle \text{sign} \rangle$  reduce exponentially to 0 as enlarging the system's size if a sign problem presents, but previous studies reveal that it is not always so [38, 58, 59]. In our investigation on non-chiral magic-angle TBG with  $\nu = -3$ , the values of  $\langle \text{sign} \rangle$  for  $L = 4, 5$  are shown in Fig. S3, where  $\langle \text{sign} \rangle$  approximates 0

when  $u_0 \geq 40$  meV and  $T = 1$  meV for  $L = 4$ . Nevertheless, judging by the stability and reproducibility of our data, physics when  $\langle \text{sign} \rangle > 0.05$  can be effectively and reliably investigated with reasonable computing resources. Thus, Green's functions for  $L = 5$  are obtained at  $T = 3$  meV, where  $\langle \text{sign} \rangle$  reaches below 0.05 when  $u_0 \in \{40, 50\}$  meV, as shown in Fig. S3 (b). Moreover, 3 meV is still well below single-particle gaps. For the cases when  $L = 3$  or  $L = 4$ , simulation temperatures can be lower (see Fig. 2 and Fig. S7).

It is quite intuitive how to avoid negative weight. Denoting  $O_C = \text{Tr}(U_C O) / \text{Tr}(U_C)$ ,  $\langle O \rangle$  can be rewritten as

$$\begin{aligned}
 \langle O \rangle &= \frac{\sum_C O_C P_C}{\sum_C P_C} \\
 &= \frac{\sum_C O_C \text{sgn}(P_C) |P_C| / \sum_C |P_C|}{\sum_C \text{sgn}(P_C) |P_C| / \sum_C |P_C|}
 \end{aligned} \tag{12}$$

Thus, the numerator and the denominator can be sampling separately by  $|P_C| / \sum_C |P_C|$  or  $|P_C|$ , with  $O_C \text{sgn}(P_C)$  and  $\text{sgn}(P_C)$  being the measured quantities, and  $\langle O \rangle$  can be further obtained.



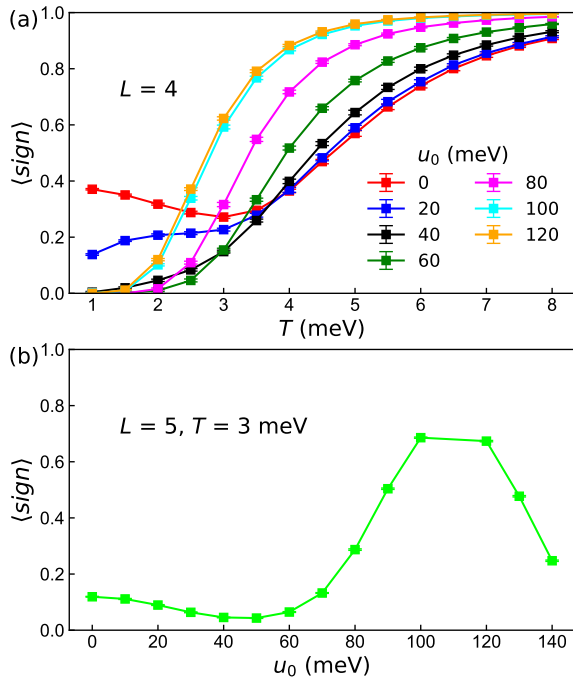


FIG. S3.  $\langle sign \rangle$  of magic-angle TBG with  $\nu = -3$ , when (a)  $L = 4$  varying with  $T$  and  $u_0$ , and (b)  $L = 5$  and  $T = 3$  meV varying with  $u_0$ .  $\langle sign \rangle$  reaches 0 when  $u_0 \geq 40$  meV as  $T = 1$  meV for  $L = 4$  in (a), while  $\langle sign \rangle$  is below 0.05 when  $u_0 \in \{40, 50\}$  meV for  $L = 5$  and  $T = 3$  meV in (b).

### III. Imaginary Green's function and derived gaps

The decaying of  $G(\Gamma, \tau)$  is depicted in Fig. S4, where the convergence of decaying can be seen with increasing  $L$ . The single-particle gaps can be obtained by fitting  $G(\tau) = \exp(-\Delta\tau)/2 + \exp(-\Delta(\beta - \tau))/2$  to the data in a range with linear  $\tau$ -dependence of logarithmic GFs as shown in Fig. S4, and the obtained gaps are demonstrated in Fig. S5, where those of other  $\mathbf{k}$  points are also shown. Here  $\Delta$  refers to the minimum gap for each  $\mathbf{k}$  point.

The gaps of  $L = 3$  from ED, considering the computational complexity, is calculated as well and shown in Fig. S6 (green squares), where counterparts from QMC (red and blue squares), with the simulation temperature being 2 and 3 meV, respectively, are also shown. As the result from ED is of ground state, gaps from QMC at 3 meV are lower than those from ED, and the lowering of simulation  $T$  can reduce the deviation, as proved by those of  $T = 2$  meV. Besides, the same tendency is obtained that the gap closes at  $u_0 \approx 0.8u_1$ . In addition, the detail of implementation of ED is depicted in Sec. VII.

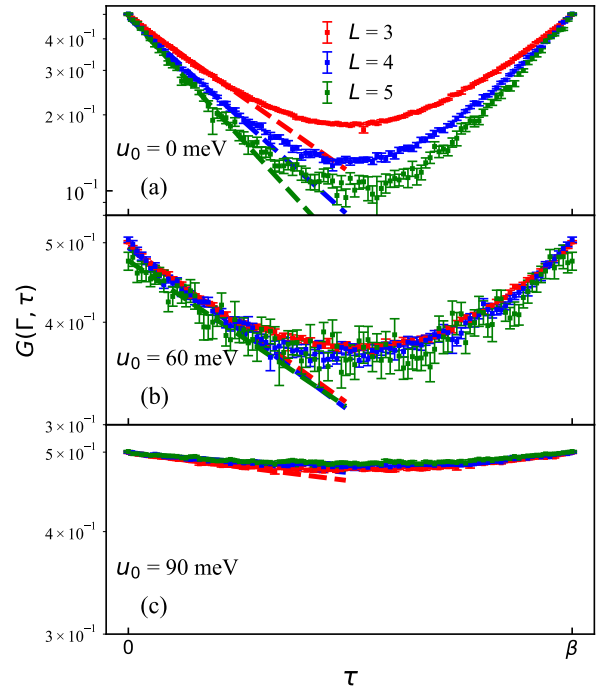


FIG. S4. Decaying of imaginary time Green's function of  $\Gamma$  point with  $L = 3, 4, 5$ , when (a)  $u_0 = 0$  meV, (b)  $u_0 = 60$  meV, and (c)  $u_0 = 90$  meV, where the log scale is used. Mind that the vertical scales of (b) and (c) is different from that of (a). The fitting dashed lines are also shown in each panel, the slopes of which give the single-particle gaps in Fig. 1 (b) in the main text and Fig. S5.

### IV. Chern polarization and finite size scaling

A perturbation term, which reads

$$\delta H = \begin{pmatrix} 0 & 0 \\ 0 & \delta\sigma_z \end{pmatrix}, \quad (13)$$

with  $\delta = 1$  meV and  $\sigma_z$  being third Pauli matrix, is added to the bottom layer of  $H_0$  to obtain a well defined Chern basis  $|\psi\rangle$ . This perturbation term acts the role of the hexagonal boron nitride on a bottom gated TBG [64]. It breaks  $C_{2z}\mathcal{T}$  but not  $\mathcal{T}$ , which means spontaneous time symmetry breaking is still allowed. Denoting the original basis as  $|\phi\rangle$ , the imaginary Green's function in the Chern basis can thus be related to the counterpart of the original basis, by  $\langle\psi|G(\mathbf{k})|\psi\rangle = \langle\psi|\phi\rangle\langle\phi|G(\mathbf{k})|\phi\rangle\langle\phi|\psi\rangle$ . The QAH order parameter is defined as  $P_C/N_{\mathbf{k}}$ , where  $P_C = N_+ - N_-$  and  $N_m = \sum_{\mathbf{k}} c_{\mathbf{k},m}^\dagger c_{\mathbf{k},m}$ . The correlation function of this QAH order, or Chern number polarization, is defined as  $S \equiv \langle(N_+ - N_-)^2\rangle/N_{\mathbf{k}}^2$  and can be calculated in the Chern basis, whose values are shown in Fig. 2 and Fig. S7.

Finite-size scaling is used to determine the critical temperature ( $T_c$ ) of the QAH transition, as shown in Fig. S7. Here the two-dimensional Ising class is employed, with the critical exponents  $\beta = 1/8$  and  $\nu = 1$  (mind that here  $\beta$  is not the inverse temperature and  $\nu$  is not the filling parameter), which obeys

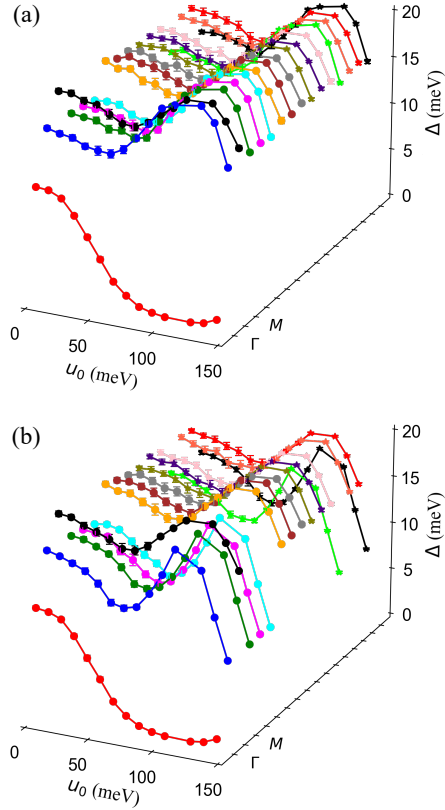


FIG. S5. Gaps of two bands,  $\pm$ , (a) and (b), of  $\mathbf{k}$  points in MBZ with  $L = 4$  and varying  $u_0$ . Here  $\Gamma$  and  $M$  refer to the red circle-line and the black circle-line, respectively, and the rest circle-lines or star-lines are those of the rest momentum points. Note that the gaps of - band remain quite large values ( $> 8$  meV) when  $u_0 = 150$  meV, as shown in (b).

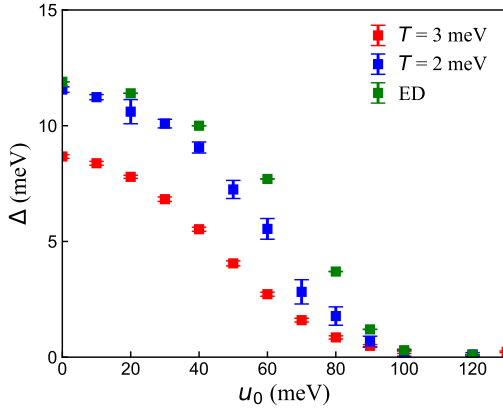


FIG. S6. Gaps from ED (green squares) when  $L = 3$  and compared with those from QMC (red and blue squares) with  $T = 3, 2$  meV, respectively.

the scaling form  $S(T, L)L^{2\beta/\nu} = f((T - T_c)L^{1/\nu})$ , where  $f$  is the scaling function [37, 38]. The derived values of  $T_c$  are shown in Fig. 1 and Fig. S7, and those of  $u_0 = 0$  is consistent with those of Ref. [37].

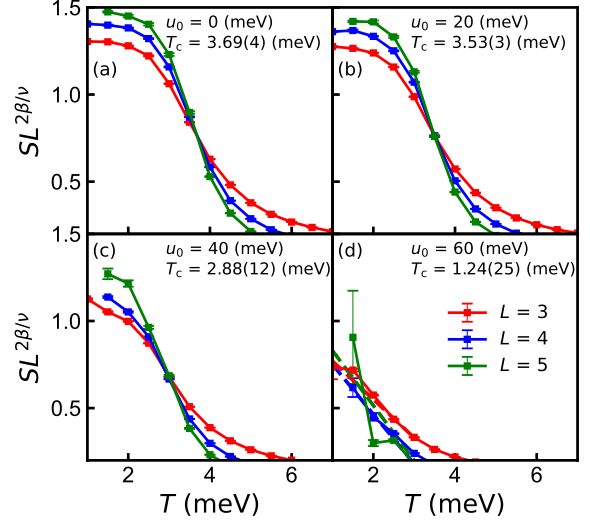


FIG. S7. Finite-size scaling of  $S$  using 2D Ising exponents and the derived  $T_c$  of various  $u_0$ , corresponding to those of Fig. 1 (a). Fitting lines are shown in (d).

## V. Verification of the semimetallic phase

Average Green's function, by summing over  $\mathbf{k}$  points, and  $LDOS$  are demonstrated in Fig. S8, where  $u_0 = 90$  meV. The convergence of decaying of  $G(\tau)$  is seen, and  $G(\beta/2)$  reduces to a minimum but finite value at large  $L$  limit, as shown in (a) and (b) respectively. Meanwhile, the peak of  $LDOS$  at Fermi level decrease to a minimum but finite value as the system size being larger than 16, as depicted in (d). Moreover, the interactive dispersion shows a quadratic cone at  $\Gamma$ , which is consistent to the minimum but finite values of  $G(\beta/2)$  and  $LDOS(\omega = 0)$  of large  $L$ , confirming the semimetallic nature of this system when  $u_0 = 90$  meV.

## VI. CDW and superconductivity

The charge density wave (CDW) is suggested to exist when  $u_0 > 88$  meV by a Hartree-Fock mean field study [28]. To verify it, we calculate an analogous monolayer CDW correlation,  $S(\mathbf{q}) = \langle n_{\mathbf{q}} n_{-\mathbf{q}} \rangle$ , where  $n_{\mathbf{q}} = \frac{1}{N_{\mathbf{k}}} \sum_{\mathbf{k}, m_1, m_2} \left( \sum_{G, G', X} u_{m_1, G, X}^* (\mathbf{k} + \mathbf{q}) u_{m_2, G', X}(\mathbf{k}) \right) c_{\mathbf{k} + \mathbf{q}, m_1}^\dagger c_{\mathbf{k}, m_2}$  with  $X$  summing over  $\{A_1, A_2\}$ . However, this CDW correlation show little uprise with increasing  $u_0$  for all  $\mathbf{k}$  but  $\Gamma$ , including that of  $M$ , which is labeled by black circle-line and lacks a peak, as demonstrated in Fig. S10, which indicates the absence of CDW.

To investigate the existence of s-wave superconductivity, a pairing correlation, being defined as  $P = \langle \Delta \Delta^\dagger + \Delta^\dagger \Delta \rangle / 2N_{\mathbf{k}}^2$ , is also measured. Here  $\Delta$  is not the previous gap, and  $\Delta^\dagger = \sum_{\mathbf{k}, m_1, m_2} c_{\mathbf{k}, m_1}^\dagger c_{-\mathbf{k}, m_2}^\dagger$ . However, this pairing correla-

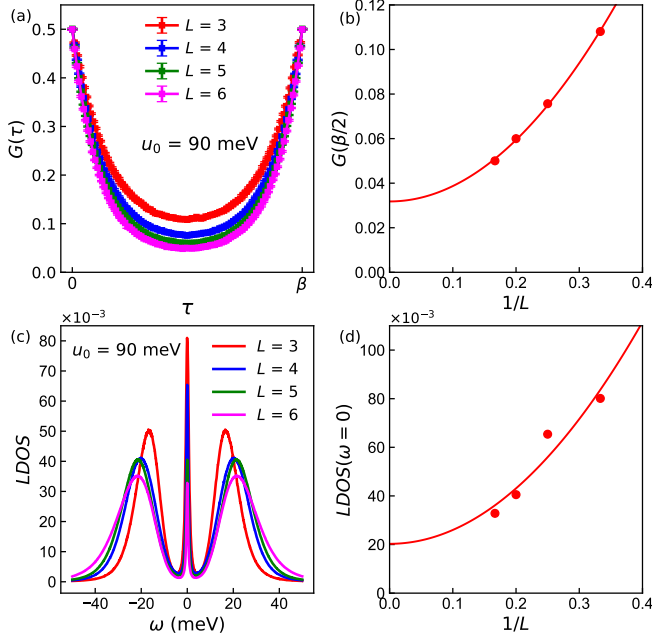


FIG. S8. The decaying of average Green's function (a) and the reducing of the peak at Fermi level of  $LDOS$  (c) with increasing system size when  $u_0 = 90$  meV. The extrapolations of  $G(\beta/2)$  and the intensity of the peaks of  $LDOS$  to larger size are shown in (b) and (d), respectively.

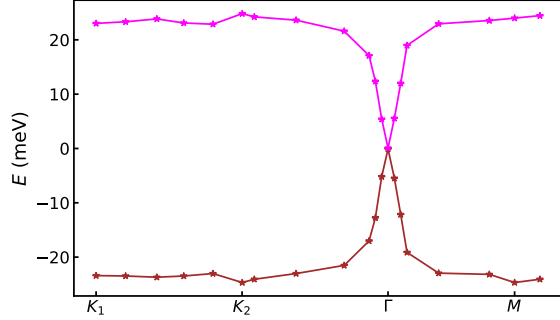


FIG. S9. Interactive dispersion when  $u_0 = 90$  meV and  $L = 5$ .

tion fluctuates at 0, as shown in Fig. S11, indicating the void of this kind of pairing or superconductivity.

## VII. Implementation of exact diagonalization

Exact diagonalization (ED) is implemented to obtain the charge gap of the system in comparison to those from QMC. For  $L \times L$  ( $\equiv N_k$ ) systems with the two nearly flat bands taken into account, there are  $2L^2$  single particle states in total which are labeled by momentum and band index. Here we use an integer  $i \in [0, 2L^2 - 1]$  to label each single particle state,  $d_i^\dagger \equiv d_{\mathbf{k}m}^\dagger$ , whose momentum  $\mathbf{k}$  and band index  $m$  are determined by  $i$ , with  $\mathbf{k}$  being inside the moiré Brillouin zone.

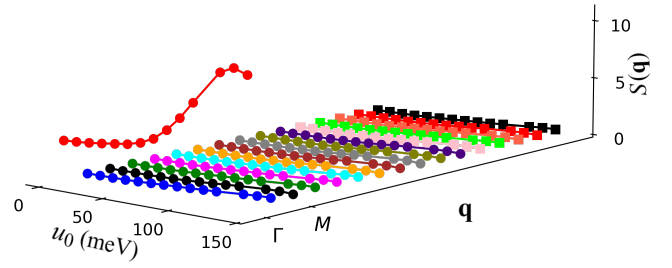


FIG. S10. The correlations of CDW order at various momentum points,  $\mathbf{q}$ , varying with  $u_0$ , where  $L = 4$ . Note that  $\Gamma$  and  $M$  refer to red-circle line and black-circle line, respectively.

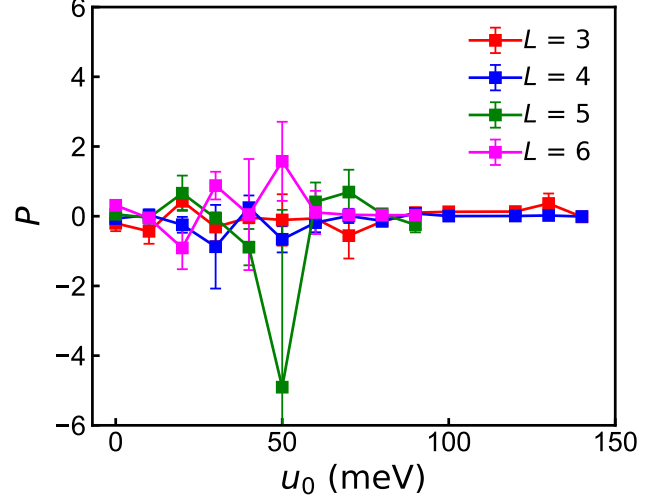


FIG. S11. The correlations of the superconducting pairing,  $P$ , with altered  $u_0$  and  $L$ .

The Hamiltonian in Eq. (6) can be rewritten in the following form by moving all electron creation operator to the left:

$$H = \sum_{i,i',j',j} V_2(i,i',j',j) d_i^\dagger d_{i'}^\dagger d_j d_j + \sum_{i,j} V_1(i,j) d_i^\dagger d_j + V_0. \quad (14)$$

The matrix element between arbitrary manybody states can be obtained from Eq.(14). Let  $|\psi\rangle$  be a simple direct product state  $|\psi\rangle = C_{i_{N-1}}^\dagger \dots C_{i_0}^\dagger |0\rangle$  whose creation operators are ordered by  $i_{N-1} > \dots > i_1 > i_0$ . Then  $|\psi\rangle$  can also be represented by a string of bits with length  $2L^2$  such as  $|1101001\dots\rangle$ . The Hamiltonian can be written in the basis made of these distinct direct product states. For a given product state  $|\psi\rangle$ , if there is another product state  $|\psi'\rangle$  such that  $\langle \psi' | H | \psi \rangle \neq 0$ , then either of the two situations occurs: (1) there exist distinct numbers  $i \neq i'$  such that  $|\psi'\rangle \propto d_i^\dagger d_i |\psi\rangle$ ; (2) there exist distinct numbers  $i, j, i', j'$  with  $i > j, i' > j'$  such that  $|\psi'\rangle \propto d_j^\dagger d_{i'}^\dagger d_i d_j |\psi\rangle$ . Then, according to Eq.(14), we have

$$\begin{aligned} \langle \psi'_2 | H | \psi \rangle = & (-1)^{\mu(i,j)} (-1)^{\mu'(i',j')} [V_2(j',i',i,j) \\ & - V_2(j',i',j,i) - V_2(i',j',i,j) + V_2(i',j',j,i)]. \end{aligned} \quad (15)$$

Here  $\mu(i, j)$  is the number of "1" between the  $i$ -th and  $j$ -th bits in the bit-representation of  $|\psi\rangle$ . This sign factor comes from the Fermi anti-commutation of creation operators. Similarly,

for  $|\psi'_1\rangle \propto d_i^\dagger d_i |\psi\rangle$ , we have

$$\begin{aligned} \langle \psi'_1 | H | \psi \rangle = & \sum_j (-1)^{\mu(i,j)} (-1)^{\mu'(i',j)} [V_2(j, i', i, j) \\ & - V_2(i', j, i, j) - V_2(j, i', j, i) + V_2(i', j, j, i)] \\ & + V_1(i', i). \end{aligned} \quad (16)$$

The diagonal matrix elements are

$$\begin{aligned} \langle \psi | H | \psi \rangle = & V_0 + \sum_{i>j, \psi_i=\psi_j="1"} [V_2(j, i, i, j) - V_2(j, i, j, i) \\ & - V_2(i, j, i, j) + V_2(i, j, j, i)] + \sum_{i, \psi_i="1"} V_1(i, i). \end{aligned} \quad (17)$$

The charge gap in Fig.S6 is the energy difference between  $(N_k + 1)$ -particle system and  $N_k$ -particle system.